

# Damage detection techniques for structural health monitoring of bridges from computer vision derived parameters

Chidiebere B. Obiechefu<sup>1</sup> and Rolands Kromanis<sup>\*2</sup>

<sup>1</sup> School of Architecture, Design, and the Built Environment, Nottingham Trent University, United Kingdom

<sup>2</sup> Department of Civil Engineering, Faculty of Engineering Technology, University of Twente, Netherlands

(Received October 15, 2020, Revised December 29, 2020, Accepted January 4, 2021)

**Abstract.** The paper presents damage detection techniques for structural health monitoring of bridges incorporating computer vision derived measurements. The feasibility of the techniques is demonstrated on a numerical model of a bridge girder. The girder is subjected to a load induced by a slowly moving truck. Multiple damage scenarios are simulated. Damage detection is carried out on the four types of response (i.e., deflection, inclination angle, strain and curvature) computed from the numerical model. The robustness of vision measurement approach for damage detection is validated at different levels of added measurement noise. The noise is expressed as the pixel resolution achievable with the image processing algorithm at multiple camera field of views applied to target motions. Damage detection and location accuracies are influenced by damage extent, added measurement noise and type of response. The study shows that deflections and strains outperform inclination angles and curvatures detecting damages in noisy measurements. Strains are the best type of response for damage detection and location when high measurement resolutions (e.g., 1/500 pixels) can be achieved.

**Keywords:** damage detection; numerical modelling; data interpretation; signal processing; vision-based measurement

---

## 1. Introduction

Bridges are vital elements of civil infrastructure. Their continuous and safe operation is important for their users and avoidance of delays and detours. Bridge condition assessment predominantly relies on regular visual bridge inspections, which are time and labour consuming, and subjective (Brownjohn 2007). Delays in detecting and recognizing structural faults or damages can be expected, especially considering that principal inspections, during which an inspection team accesses and examines critical components of the bridge within a touching distance, are carried out every six years (Highways Agency *et al.* 2018). For example, the London's Hammersmith flyover was suddenly closed for emergency repairs in December 2011 following an inspection, in which an already substantial cable corrosion and weakening caused by water ingress were discovered (Transport for London 2011). Bridge inspections can be complemented with the analysis of structure's load and response mechanism, which can be obtained using suitable monitoring systems. Usually, monitoring systems employ contact sensors

---

\*Corresponding author, Assistant Professor, E-mail: [r.kromanis@utwente.nl](mailto:r.kromanis@utwente.nl)

such as fibre optic sensors, inclinometers, and strain gauges (Reagan *et al.* 2018). Sophisticated and dense sensor systems are installed on important bridges to the nation's infrastructure. For example, the Queensferry Crossing in Scotland is equipped with approximately 1,000 sensors monitoring wind, temperature, corrosion, motion and strain (Infrastructure Intelligence 2017).

The installation, operation and maintenance of monitoring systems are expensive, therefore, bridge condition assessment of short to medium span bridges with a low volume of traffic still relies predominantly on visual inspections (Brownjohn *et al.* 2016). For example, the cost of installing a structural health monitoring (SHM) system (in 2008) on the new I-35W St. Anthony Falls Bridge in the USA cost \$73,000, with further annual maintenance costs of \$35,000 (Dalia *et al.* 2018). These prohibitive costs present an opportunity for cost-effective monitoring systems offering reliable condition assessment of bridges. Vision-based monitoring systems, which consists of a fixed image acquisition device(s) and image processing software, have vast potential to become ubiquitous SHM systems (Lydon *et al.* 2019, Shao *et al.* 2020). Setting up a camera system, in general, requires no working at heights nor direct access to the bridge, and causes no or little traffic disruptions.

Measurement collection with and applications of computer vision (CV) systems for bridge monitoring have been well researched at local and global levels (Xu and Brownjohn 2017, Feng and Feng 2018, Dong and Catbas 2020). Professional cameras with adequate lenses, camcorders, action cameras and smartphones are all suitable for accurate measurement collection (Zaurin and Catbas 2010, Fukuda *et al.* 2013, Brownjohn *et al.* 2017, Kromanis *et al.* 2019). Structural response is extracted from image frames of a bridge under loading using either proprietary software (e.g., Video Gauge™ (Imetrum 2020)), open source software (e.g., QUBDisp (Lydon *et al.* 2019) and DeforMonit (Kromanis and Al-Habaibeh 2017)) or other image processing algorithms that detect and track targets in image frames. The majority of studies have focussed on displacement measurement of a single target (i.e., localised sensing) on a bridge (Ribeiro *et al.* 2014). For example, Khuc and Catbas (2017) employed fast retina key-point algorithm to match detected key points at a nut on a steel girder. Brownjohn *et al.* (2017) used the Dynamic Monitoring System with a template matching and super resolution image-based patented algorithm (Potter and Setchell 2014, Imetrum 2020) to measure mid-span deflections of the Humber and Tamar bridges. However, one of the main strengths of vision-based monitoring is the ability to track motions of multiple targets (i.e., distributed sensing) (Ji *et al.* 2020, Xu *et al.* 2018). Limitations for the achievable measurement resolution can depend on, but are not limited to, the image processing algorithm and camera field of view. For example, reasonable measurement accuracies, while capturing the entire bridge in a single field of view with cost-effective cameras, can be achieved only for short span bridges with high deflections (Xu *et al.* 2018, Chu *et al.* 2019, Kromanis 2020). However, accurate response measurement along the length of the entire bridge is required for accurate condition assessment of bridges.

Measurement collection and analysis approaches are decided upon the bridge testing method: dynamic (e.g., vibration-based), static (e.g., traffic) and quasi-static (e.g., temperature). Dynamic testing is the most developed method for vibration-based damage identification in bridges (Doebbling *et al.* 1998). However, it has some limitations and certain conditions must be satisfied to achieve accurate and reliable results. Firstly, very high measurement accuracy has to be achieved to capture higher order vibration modes, which may require employment of multiple synchronized cameras. Secondly, temperature affect vibration properties, therefore requiring temperature measurements, preferably distributed temperature measurements. Although these requirements can be met, they may imply high costs and may be challenging at in-situ conditions. Quasi-static

testing requires long-term measurements. Only a few studies have explored performance of long-term videogrammetry (Park *et al.* 2015, Zhou *et al.* 2019), which is still in its infancy and, therefore, outside of the scope of the study. Static testing maintains the advantage of requiring only stiffness properties, which can be obtained easily and may yield more reliable results for damage detection than dynamic testing (Bakhtiari-Nejad *et al.* 2005).

In static testing, structural displacements, strains, inclination angles and curvatures form the basis for damage detection (Chen *et al.* 2005, Gauthier *et al.* 2008, Abdo 2011, Kromanis and Liang 2018). Curvatures, and inclination angles, for example, are derivatives of deflections, which are directly related to bending moment and flexural rigidity. A change in the flexural rigidity affects structural response, which indicates a change in bridge conditions. This relationship can be exploited for damage detection. The performance of condition assessment methods is firstly studied on numerical models, then employed in the laboratory environment and, finally, considered for the use on full-scale structures.

Chen *et al.* (2005) proposed a damage localisation and structural identification technique that utilises the Grey relation coefficient. This technique detects and defines outliers as a damage sensitive feature in the curvature of the beam along its length. The technique was validated on a numerical model of a cantilever beam showing that as little as 7% stiffness loss of a section is detected, located and quantified. Abdo (2012) carried out a numerical study for two types of beams using the Grey relation analysis to detect and located damages from displacement curvatures. The robustness of the method was also tested with added measurement noise. Lee and Eun (2008) introduced an analytical method for damage detection by utilizing displacement curvature. The method was validated on 1.0 m long cantilever beam with sever damages, i.e., 67% stiffness loss and measured by four displacement sensors. These techniques require high measurement accuracy and were not evaluated using a computer vision-based system, which may produce measurement errors hindering structural damage.

Recent studies have also investigated the feasibility of computer vision-based SHM. Feng *et al.* (2015) developed a vision sensor for multipoint displacement monitoring based on an advanced template matching algorithm. Feng and Feng (2016) employed the vision sensor to verify the feasibility of output-only damage detection using vehicle-induced displacements and mode shape curvature index in a laboratory study. A 1.6 m simply supported steel beam was excited with hammer impacts at intact and damage states (20% section stiffness reduction). Damage location was accurately detected. However, the motion range of vertical displacements at the midspan was almost 30 mm (i.e., 15 mm amplitude). 15 mm deflection in 1.6 m is  $L/106$ , where  $L$  is the length of the span. Erdenebat *et al.* (2018) proposed the deformation area difference (DAD) method using deflections, inclination angles and curvatures for condition assessment of bridges. The method resolves the problem of unknown initial structural conditions by using numerical or theoretical models with known initial conditions as a reference system. The method is able to detect local stiffness reductions starting from 23.8% as validated using numerical and laboratory models with vision-based measurement (Erdenebat *et al.* 2018, 2019). The application of the DAD method was also demonstrated on a newly constructed bridge, where, of course, no damage was detected (Erdenebat and Waldmann 2020). The method is suitable for load tests, when the applied load remains stationary, while a multitude of images of parts of the bridge with bar-coded targets are captured. The images are later stitched using a proprietary software from which target displacements are computed. The photogrammetry method is not applicable for collecting measurements while vehicles are crossing the bridge. The method also did not include strain measurements as a damage sensitive feature. The implementation of some of the reviewed

methods may require much information about the structure (e.g., material properties, boundary conditions, geometry) and load on it (e.g., load location, amount, distribution). A bridge condition assessment approach (i.e., measurement collection and interpretation) requiring as little information about the structure and its geometry as possible, but being accurate and reliable for damage identification, therefore is sought by researchers and is attractive for asset owners.

In this paper, a damage detection approach for CV-SHM of bridge condition assessment is proposed and validated on a numerical model. The premise is that accurate structural response of short to medium span bridges can be obtained with cost-effective cameras and available image processing algorithms. Response is measured along the length of the entire bridge. Provided that the required measurement resolution is achieved, the performance assessment (damage detection) of the bridge can be carried out at regular inspections, maintenance or safety monitoring events. The approach is validated on a numerical model, which is a girder of a single span concrete bridge found in highways. The robustness of damage detection is assessed using multiple damage scenarios and added measurement noise, which is inevitably present in field measurements. The requirements of measurement resolution for in-situ applications are discussed, and conclusions are drawn.

## 2. Computer vision-based SHM of bridges

A damage detection approach for CV-SHM of bridges is proposed. Fig. 1 illustrates the steps in the approach. Consumer-grade cameras such as action cameras and smartphones are used during bridge inspections or other measurement collection events to capture image frames of a bridge subjected to known loads (e.g., load truck). Cameras are focused on either the entire bridge or at a selected part(s) of it. Structural response such as deflection and strain, along the length of the bridge, is computed from each image frame. Absolute maximum response values at each target location are extracted. These form the bridge response along its length; from here on referred to as bridge response. The bridge response at the first inspection is assumed to represent baseline conditions of the bridge. In each new measurement collection event, bridge response is obtained and compared to baseline bridge response for condition assessment. Collected data is stored for the asset owner's reference and retrieved when needed. The derivation and analysis of response for condition assessment are described in the following sections.

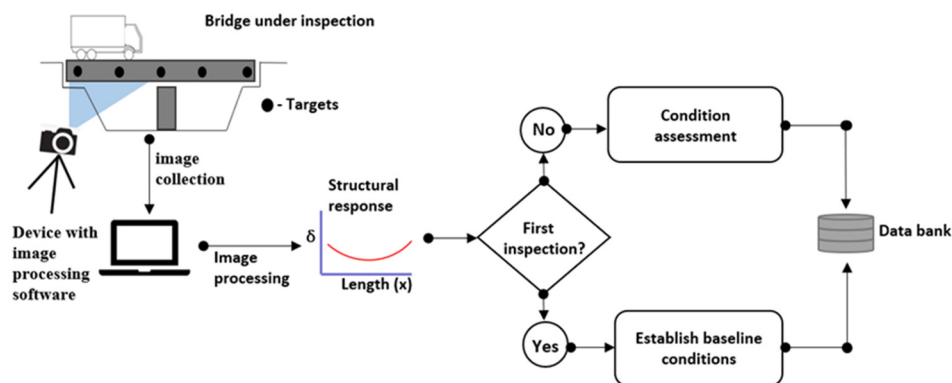


Fig. 1 Vision-based condition assessment of bridges

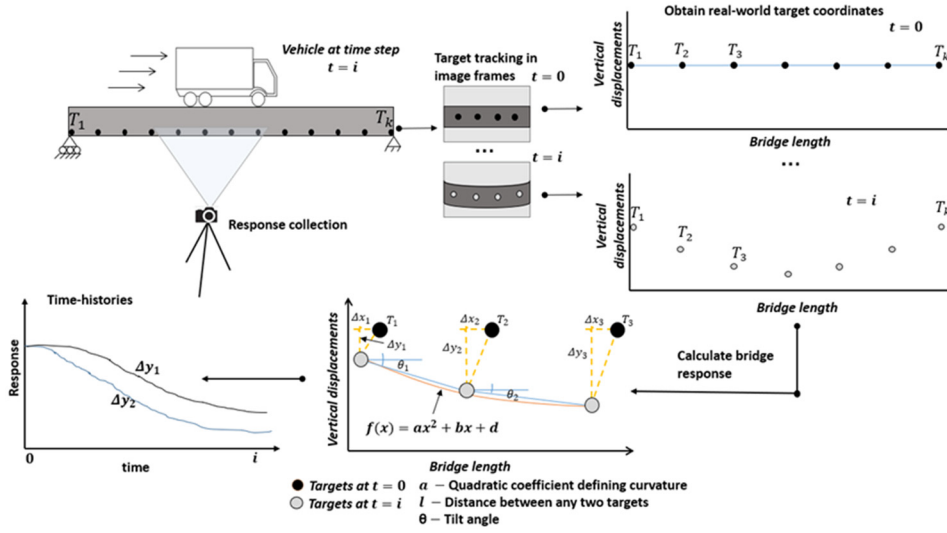


Fig. 2 Generation of structural response

## 2.1 Structural response

Fig. 2 illustrates the computation of response for computer vision-based monitoring. Image frames of a bridge under traffic loads are collected. A target displacement, which is the movement that a target ( $T$ ) makes between time step  $t = 0$  and  $t = i$ , is calculated by analysing frames with image processing algorithms and software such as Moir method (Ri *et al.* 2020), QUBDisp, DeforMonit and VG software (Kromanis *et al.* 2019). Structural response (in this study: deflection, inclination angle, strain and curvature) is computed from displacements of targets. Vertical deflections ( $\delta$ ) are products of displacements of a single target in y-axis and a scale factor (SF), which converts pixels to engineering units (e.g., mm). Strains ( $\varepsilon$ ) and inclination angles ( $\theta$ ) are derived from movements of a target pair. The derivation of a curvature function requires at least three targets. Strains, inclination angles and curvatures can be computed for any combination of targets. Time-histories for all response types and target combinations are created and prepared for bridge condition assessment. Steps involved in the derivation of all types of response are discussed below.

**Vertical deflections.** Displacements of a target in each image frame (time step), when converted to engineering units, are deflections of the structure at the location of measurement collection. For horizontal structures, vertical deflections ( $\delta$ ) are considered. A change of a target position in y-axis ( $\Delta y_i$ ), which is calculated from the target location in the first and  $i^{\text{th}}$  image frames ( $y_0$  and  $y_i$ ), assuming that pixels are converted to engineering units, is  $\delta$  at  $i^{\text{th}}$  time step (see Eq. (1)).

$$\delta_i = \Delta y_i = y_0 - y_i \quad (1)$$

**Strains.** Strain ( $\varepsilon$ ) is measured for a pair of targets. Eq. (2) can be used to calculate  $\varepsilon$  at  $i^{\text{th}}$  time step ( $\varepsilon_i$ ), which is the change of the length ( $\Delta l$ ) over the original length ( $l_0$ ) between two targets  $T_k$  and  $T_m$ . The distance between targets (or length  $l$ ) is computed from their  $x$  and  $y$  coordinates (see Eq. (3)). Strain is unitless, therefore,  $x$  and  $y$  coordinates can be either in pixel

or other measurement space.

$$\varepsilon_i = \frac{\Delta l_i}{l_0} = \frac{l_i - l_0}{l_0} \quad (2)$$

$$l = \sqrt{(x_{Tk} - x_{Tm})^2 + (y_{Tk} - y_{Tm})^2} \quad (3)$$

**Inclination angles.** The angle (tangent relationship) ( $\alpha$ ) between two targets  $T_k$  and  $T_m$  is computed using Eq. (4).  $\theta_i$  is the residual between  $\alpha$  in the first and  $i^{\text{th}}$  time steps (see Eq. (5)).

$$\alpha = \tan^{-1} \left( \frac{y_{Tk} - y_{Tm}}{x_{Tk} - x_{Tm}} \right) \quad (4)$$

$$\theta_i = \alpha_0 - \alpha_i \quad (5)$$

**Curvatures.** The curvature technique involves fitting a curve on a set of coordinate points of at least three targets. In this study, a univariate quadratic function is considered (see Eq. (6)), which is suitable for deriving the quadratic coefficient ( $a$ ), linear coefficient ( $b$ ) and constant ( $d$ ) representing a curve fitted on three points of interest (or targets).  $a$  determines the degree of curvature of the quadratic fit, therefore, it becomes the damage-sensitive feature. Any target combination is possible. The curvature ( $c$ ) for  $i^{\text{th}}$  time step is the residual of quadratic coefficients at the first and  $i^{\text{th}}$  time step (see Eq. (7)).

$$f(x) = ax^2 + bx + d \quad (6)$$

$$c_i = a_0 - a_i \quad (7)$$

## 2.2 Damage detection and location

Damage sensitive feature ( $e_{r,j}$ ) is derived from bridge response at any location. It expressed as the ratio of the change in bridge response ( $\Delta r_j$ ), which is the difference between the baseline bridge response ( $r_0$ ) and new bridge response ( $r_j$ ), to  $r_0$  (see Eq. (8)). The response symbol is set as the subscript to differentiate between types of response. For example,  $e_{\delta,j}$  is the damage feature derived from deflection ( $\delta$ ) at the  $j^{\text{th}}$  measurement collection event.  $e \approx 0$  indicates that the performance of the structure has not changed.  $e \gg 0$  indicates that the structure is damaged. Damage indicating threshold(s) ( $\gamma$ ) can be case-specific. In this study, the structure is said to be damaged if  $e > 5\%$ . Damage is located where  $e$  values spike.

$$e_{r,j} = \frac{\Delta r_j}{r_0} = \frac{r_j - r_0}{r_0} \quad (8)$$

An illustrative example of damage detection technique from the vision measurement is given in Fig. 3. Bridge vertical deflection is measured at a number of targets. Deflections along the length of the bridge are computed for each measurement step  $t$ . The maximum deflection ( $\delta_{max}$ ) value at each target location, which is the maximum structural response at a target (i.e.,  $r_{max}$ ), is extracted.  $r_{max}$  values form the deformed shape of the bridge along its length, which here is referred to as

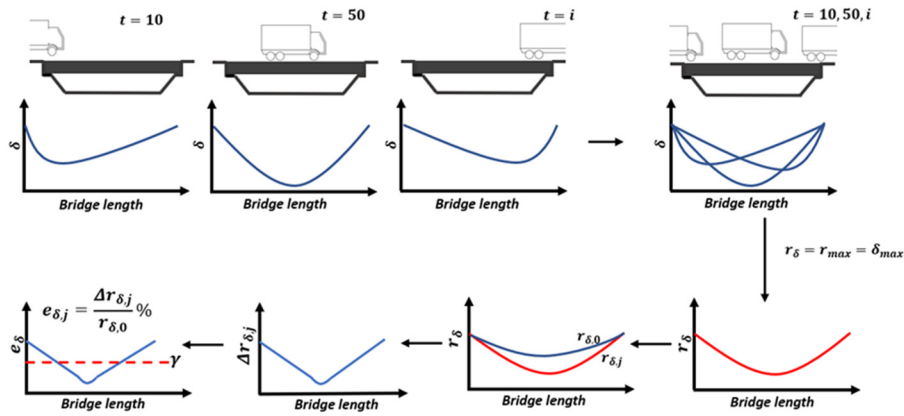


Fig. 3 Damage detection technique from vertical deflections

bridge response ( $r_\delta$ ). This also applies to other types of response such as strains, inclination angles and curvatures. Bridge response at the first measurement collection event is set as the baseline bridge response ( $r_{\delta,0}$ ), against which other bridge response measurements ( $r_{\delta,j}$ ) are evaluated (see Eq. (8)). Damage feature ( $e_\delta$ ) is calculated from  $r_{\delta,0}$  and  $r_{\delta,j}$ . It is assessed for damages by setting a threshold  $\gamma$ .  $e$  values exceeding  $\gamma$  indicate the damage location(s).

### 2.3 Measurement pre-processing

In-situ vision measurements are accompanied with measurement noise. Some of the factors influencing measurement quality are camera stability, camera field of view and resolution, pixel resolution of the image processing algorithm, and environmental effects (e.g., haze, reflection, shade). It is therefore imperative to treat target displacement histories for noise. This can be done by applying suitable moving average filters, firstly, to the displacement (in  $x$  and  $y$  axes) measurements and, lastly, to the derived response measurement. Only after response is pre-processed, the bridge response ( $r$ ) can be computed.

## 3. Numerical study

A numerical model is employed to validate the proposed approach. A girder of a bridge, which is subjected to a truck load and six damage scenarios, is introduced. Response is generated and analysed. Different intensities of measurement noise are added to the response to represent realistic in-situ measurements. Noisy response is denoised and analysed.

### 3.1 Numerical model

The model is a simply supported beam structure, which is a representative of a typical reinforced concrete girder found in highway bridges. The girder is 12 m long with a depth of 1.2 m and a breadth of 0.5 m (See Fig. 4) modelled in ANSYS. It has four rows of 50 eight-node plane stress elements (Plane 183, ANSYS Inc. (2018)). Each element is 0.24 m long, 0.3 m wide and 0.5 m thick. The bridge is subjected to a load from a slowly moving 25 tonne, three axle rigid

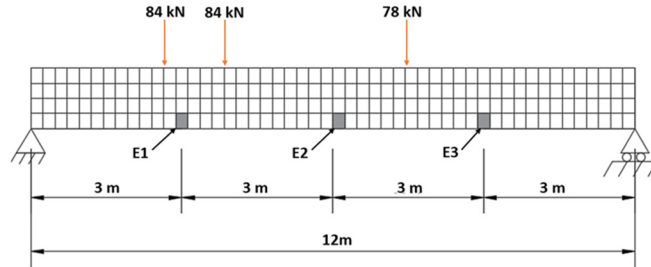


Fig. 4 A sketch of the numerical model and load locations at 50th measurement step

Table 1 Damage location scenarios

Damage location scenario	$D_1$	$D_2$	$D_3$	$D_4$	$D_5$	$D_6$
Damaged element(s)	$E_1$	$E_2$	$E_3$	$E_1, E_2$	$E_1, E_3$	$E_1, E_2, E_3$

truck. The load is distributed between several girders. The load application is simulated as a series of sequentially applied load steps. As an example, axle loads on the modelled girder at 50th load step are shown in Fig. 4.

Damage scenarios are created by reducing the value of Young’s modulus (or stiffness) of an element ( $E$ ) or a combination of elements. Fig. 4 shows selected elements for damage ( $E_i, i = 1,2,3$ ) and their locations. Six damage location scenarios ( $D_s$ ) are listed in Table 1. The reduction of element stiffness (or damage severity ( $S$ )) by 10%, 50%, and 100% are considered and referred to as  $S_1, S_2$ , and  $S_3$ . These correspond to 2.5%, 12.5%, and 25% stiffness reduction of the girder cross-section, respectively. Damage scenario  $S_1D_4$ , for example, denotes 10% reduction of stiffness in  $E_1$  and  $E_2$ . A total of 18 damage scenarios are simulated.

Nodal displacements along the bottom of the girder are extracted at each load step. Only the corner nodes of the eight-node elements are selected for the computation of response. Mid-nodes are not considered. Their nodal displacements for damaged elements have strong evidence of damage, which is immediately discernible in the bridge response along the length of the girder. The selected nodes are considered to be targets on the real structure.

Response time histories (or the influence line) derived from the target or a set of targets are shown in Fig. 5. The largest deflections (in mm), strains (in  $\mu\epsilon$ ) and curvatures (unitless, therefore

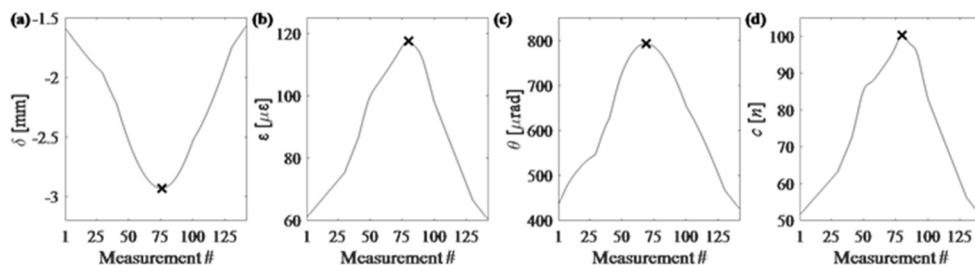


Fig. 5 Response histories of (a) deflection; (b) strain; and (d) curvature at the mid-span of the girder; and (c) inclination angle next to the left support derived from nodal displacements. ‘x’ marks the maximum absolute response value

expressed in  $n$  or 10-9) are at the mid-span of the girder. The highest inclination angles (in  $\mu\text{rad}$ ) are close to the right support of the girder.

### 3.2 Damage detection

The maximum response ( $r_{max}$ ) for each target location(s) is extracted forming the girder response ( $r$ ) along its length. Damage detection is demonstrated on all four types of response: deflection ( $r_\delta$ ), strain ( $r_\varepsilon$ ), inclination angle ( $r_\theta$ ) and curvature ( $r_c$ ). Damage scenarios  $S_1D_2$  and  $S_2D_5$  are used as demonstrators. Fig. 6 (top) plots  $r$  values along the length of the girder. Plots of  $r_\delta$  and  $r_\theta$  for undamaged and damaged girder show no discernible differences. Strains and curvatures are more sensitive to locale damages than deflections and inclination angles, which is indicated by spikes in  $r_\varepsilon$  and  $r_c$  values for the damaged structure. Spikes indicate damages and their locations. Values of inclination angle along the length of the girder change from positive (clockwise inclination) to negative (anticlockwise inclination). Inclination angles at the left support are larger than at the right support. This can be explained with the load distribution (i.e., axel loads) on the girder, see Fig. 4.

$\Delta r$  values along the length of the girder show changes in girder response, which suggest for damage(s) and its(their) location (Fig. 6 (middle)). Changes in  $\Delta r_\varepsilon$  and  $\Delta r_c$  are significant for  $S_2D_5$ , but for  $S_1D_2$  the peak at the middle of the girder is small (although noticeable).  $\Delta r_\delta$  for  $S_1D_2$  spikes, though with a small maximum value, at the mid-section of the girder, where the damage is located.  $\Delta r_\delta$  indicates damage location for  $S_2D_5$ , when it peaks between 3 m and 9 m of the girder length.  $\Delta r_\theta$  for both damage scenarios shifts abruptly at damage locations. The trend of  $\Delta r_\theta$  is different from the others, therefore a different technique for generating the damage sensitive feature ( $e_\theta$ ) is required.

Fig. 6 (bottom) plots values of the damage sensitive feature along the length of the girder. Damage threshold  $\gamma$  is set at 5%.  $e_\delta$  for  $S_1D_2$  and  $S_2D_5$  do not exceed 2%, which indicates that the damage sensitive feature does not exceed the confidence bound. Although  $e_\delta$  peaks at damage locations.  $e_\varepsilon$  for both selected damage scenarios exceed  $\gamma$ . The peaks correctly indicate damage locations. Damage in  $S_1D_2$  is not significant enough for  $e_c$  to exceed  $\gamma$ , however, for  $S_2D_5$ ,  $e_c$  surpasses  $\gamma$  significantly at both damage locations.

A case-specific derivation of  $e_\theta$  is proposed in Eq. (9). A moving window approach is employed to obtain  $e_{\theta,g}$  at the  $g^{th}$  response measurement location along the length of the girder.  $e_\theta$  is computed as the ratio of the range of  $\Delta r_\theta$  ( $q_n$ ) to the mean of  $r_\theta$  ( $\bar{r}_\theta$ ) for  $n$  number of consecutive response measurements. To compute  $e_\theta$  at the  $g^{th}$  response location, values to its left and right are selected so that the  $g^{th}$  response location is in the middle. Therefore  $n$  needs to be an odd integer, larger or equal to 3. Large  $n$  values round  $q_n$  and  $\bar{r}_\theta$  hindering damage locations, thus damages close to supports may not be revealed. However small  $n$  values can be sensitive to small, local changes to the response and provide  $e_\theta$  values that frequently exceed the damage threshold. The selection of  $n$  depends on the number of distributed targets ( $f$ ) on the structure and distance between them. In this study  $n$  is set to 5. Although  $e_\theta$  peaks above 2% at damage locations for both scenarios, the damage threshold is not breached.

$$e_{\theta,g} = \frac{q_{n,g}}{\bar{r}_{\theta,n,g}}, \begin{cases} \frac{(n-1)}{2} < g < f - \frac{(n-1)}{2} \\ n \geq 3 \\ n = \{2k + 1 : k \in \mathbb{Z}\} \end{cases} \quad (9)$$

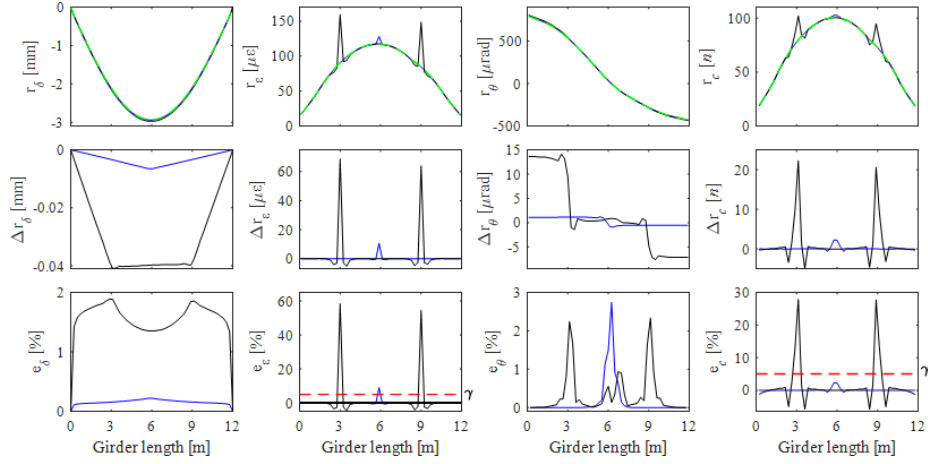


Fig. 6 From left to right: deflection, strain, inclination angle and curvature along the length of the girder. From top to bottom: girder response ( $r$ ), change in girder response ( $\Delta r$ ) and damage sensitive feature ( $e$ ). Green dashed lines are response at no damage (only for response plots); blue and black lines are  $S_1D_2$  and  $S_2D_5$ , respectively

Table 2 Summary of damage detection

Damage feature	Damage severity	$D_1$	$D_2$	$D_3$	$D_4$	$D_5$	$D_6$
$e_\delta$	$S_1/S_2/S_3$	N/N/Y	N/N/Y	N/N/Y	N/N/Y	N/N/Y	N/N/Y
$e_\epsilon$	$S_1/S_2/S_3$	Y/Y/Y	Y/Y/Y	Y/Y/Y	Y/Y/Y	Y/Y/Y	Y/Y/Y
$e_\theta$	$S_1/S_2/S_3$	N/N/Y	N/Y/P	N/N/P	N/P/Y	N/N/P	N/P/Y
$e_c$	$S_1/S_2/S_3$	N/Y/Y	N/Y/Y	N/Y/Y	N/Y/Y	N/Y/Y	N/Y/Y

Y – damage is detected; P – damage is partly detected; N – damage is not detected;

$$q_{\theta,n,g} = \max_{l,m=1,\dots,n} (\Delta r_{\theta,g-l-1} - \Delta r_{\theta,g-m-1}) \quad (10)$$

$$\bar{r}_{\theta,n,g} = \frac{1}{n} \sum_{l=1}^n |r_{\theta,g-l-1}| \quad (11)$$

The summary of damage detection is given in Table 2. If  $e_r$  exceeds the damage thresholds at the damage location(s), the damage is said to be detected, if it does not then the damage is not detected. In instances when  $e_r$  surpasses damage thresholds at no damage locations and also location where damages are created, damage is said to be partially detected. An example is  $e_\theta$  for  $S_3D_5$ , which is similar to  $S_2D_5$  (see Fig. 6), however,  $e_\theta$  values at 6 m length exceed the damage threshold although the girder is not damaged at its midspan.

### 3.3 Added measurement noise

Camera specifications are important for achieving accurate response measurements, which are compulsory for a reliable assessment of bridge conditions. This section investigates the choice of

the camera field of view and desirable measurement resolution. The increase of the field of view results in the decrease of the measurement resolution, i.e., increase of the measurement noise ( $\eta$ ). The achievable pixel resolution of the image processing algorithm is as important as the selection of the suitable field of view. Image processing algorithms are reported to achieve resolution between 1/2 and 1/100 pixels (further referred to as  $\frac{1}{100}px$ ) (Feng *et al.* 2015), and claimed to reach even  $\frac{1}{500}px$  resolution using a patented algorithm (Potter and Setchell 2014, Imetrum 2020).

Results from Section 3.1 and 3.2 are used to guide the selection of  $\eta$ . It is added to  $x$  and  $y$  displacements of each target (i.e., nodal displacements of the numerical model), which are used to derive girder response, at each load step.  $\eta$  is the product of the scale factor ( $SF$ ) and pixel resolution ( $PR$ ) (Eq. (12)).  $SF$  is the quotient of distance on the image ( $d$ ) and known physical dimension ( $D$ ), which here is expressed as millimetres per pixel (mm/px).

$$\eta = SF \cdot PR \quad (12)$$

$$SF = \frac{D}{d} \quad (13)$$

The assumption is made that monitoring is performed with a 12 MP camera(s) ( $4096 \times 3072$  pixel frame), which is(are) set perpendicular to the mid-span of the girder. Vertical and horizontal scale factors are assumed to be the same. Two horizontal field of views ( $F_1 = 12m$  and  $F_2 = 2.4m$ ) are selected.  $F_1$  covers the entire length of the girder.  $SF$  for  $F_1$  is 2.93 mm/px, as calculated using Eq. (13). With 1/500 pixels resolution  $\eta$  is no larger than  $5.9 \times 10^{-3}$  mm. The distance ( $D$ ) between targets is 240 mm limiting the maximum strain error to  $\frac{5.9 \times 10^{-3} mm}{240 mm} \times 10^6 = 25 \mu$ . Such measurement accuracy is not sufficient for the detection of damages at  $S_1$ . The measurement accuracy for  $F_2$  is five times higher, giving  $SF = 0.6$  mm/px,  $\eta \leq 1.2 \times 10^{-3}$  mm and maximum of 5  $\mu$  error. With  $F_2$  at least five cameras are required to capture response of the entire girder.

$\frac{1}{500}px$  is the maximum cited measurement resolution (Potter and Setchell 2014, Imetrum 2020). Achieving such high accuracy in-situ is challenging, therefore, three  $PR$ s,  $\frac{1}{500}px$ ,  $\frac{1}{100}px$  and  $\frac{1}{20}px$ , are studied. They form three measurement noise level ( $N_i, i = 1,2,3$ ), which are added to displacements collected at the two horizontal field of views. Combinations of added measurement noise and field of view are given in Table 3. For example,  $N_1F_1$  corresponds to  $\frac{1}{500}px$  resolution accuracy (or measurement error) derived from a horizontal field of view that captures 12 m (i.e., the entire length) of the girder.  $N_2F_2$  and  $N_3F_2$  are the same as  $N_1F_1$  and  $N_2F_1$ , respectively, therefore they are not listed in the table and included in the study.  $\eta$  limits are set in Eq. (14), and they follow random Gaussian distribution.

$$-0.5 \cdot (SF \cdot PR) < \eta < 0.5 \cdot (SF \cdot PR) \quad (14)$$

### 3.4 Response pre-processing

Raw (or, in this study, with added measurement noisy) target displacements must be pre

Table 3 Combinations of added measurement noise and camera field of view

$N_i$	$PR$ (px)	$F_1$ (the entire length of the girder)	$F_2$ (2.4 m of the girder)
$N_1$	$\frac{1}{500}$	$-\frac{5.9}{2} \cdot 10^{-3} mm < \eta < \frac{5.9}{2} \cdot 10^{-3} mm$	$-\frac{1.2}{2} \cdot 10^{-3} mm < \eta < \frac{1.2}{2} \cdot 10^{-3} mm$
$N_2$	$\frac{1}{100}$	$-\frac{29.3}{2} \cdot 10^{-3} mm < \eta < \frac{29.3}{2} \cdot 10^{-3} mm$	The same as $N_1 F_1$
$N_3$	$\frac{1}{20}$	$-\frac{146}{2} \cdot 10^{-3} mm < \eta < \frac{146}{2} \cdot 10^{-3} mm$	The same as $N_2 F_1$

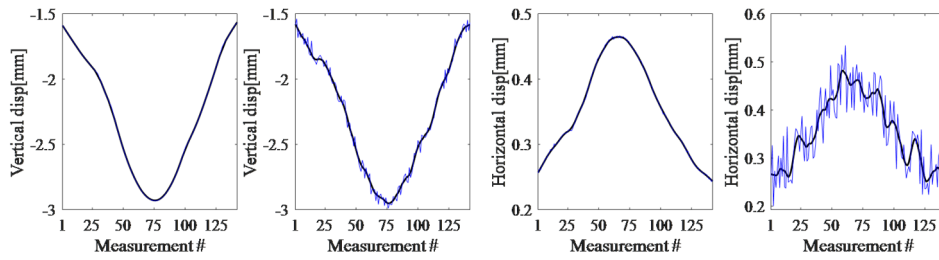


Fig. 7 Raw (blue line) and pre-processed (black line) displacements of a target at the midspan of the girder. Left to right: Vertical displacements at  $N_1 F_1$ ,  $N_3 F_1$ , and horizontal displacements at  $N_1 F_1$ ,  $N_3 F_1$

processed before structural response is derived, and the performance of the structure is assessed. In this study, response pre-processing is done in two stages. First, displacement histories (vertical and horizontal) for each target are smoothed with the moving average filter of 10 measurements. Then secondary response (i.e., strain, inclination angle and curvature) are derived from displacements. The response ( $r$ ) maybe be noisy, thus another round of measurement smoothing is applied before the change in response ( $\Delta r$ ) is computed and damage sensitive feature ( $e$ ) is derived.

Response pre-processing is demonstrated on displacements from the girder at undamaged state. Fig. 7 shows raw vertical and horizontal displacements of a target at the mid-span of the girder at  $N_1 F_1$  and  $N_3 F_1$  combinations. Displacements at  $N_1 F_1$  are very smooth with very little measurement noise in comparison to displacements at  $N_3 F_1$ . Displacements at  $N_2 F_1$  are less noisy than at  $N_3 F_1$ , but noisier than at  $N_1 F_1$ . Displacements at  $N_1 F_2$  appear to have almost no noise. For reasons of brevity plots of displacements at  $N_2 F_1$  and  $N_1 F_2$  are not shown.

Secondary response is derived from pre-processed target displacements. Fig. 8 shows raw and pre-processed maximum deflection, strain, inclination angle and curvature histories at  $N_1 F_1$  and  $N_3 F_1$ . Only deflection measurement histories at  $N_1 F_1$  and  $N_3 F_1$  are similar to deflections computed directly from nodal displacement (with no added measurement noise) of the girder (see Fig. 5). Strain and inclination measurement histories at  $N_1 F_1$  resemble those shown in Fig. 5. The derivation of curvatures need very accurate coordinates of targets, and even slightest deviations from the correct values lead to large errors, which are evident in the plots. Pre-processing response is important when selecting the absolute maximum response value, which is used for the generation of the girder response. Examples are maximum inclination angle and strain values found in response histories at  $N_1 F_1$ . Maximum values from the raw response are much higher than those of pre-processed response. For reasons of brevity discussion of response at  $N_2 F_1$  and  $N_1 F_2$  are not included. They have similar description as target displacements for the two combinations

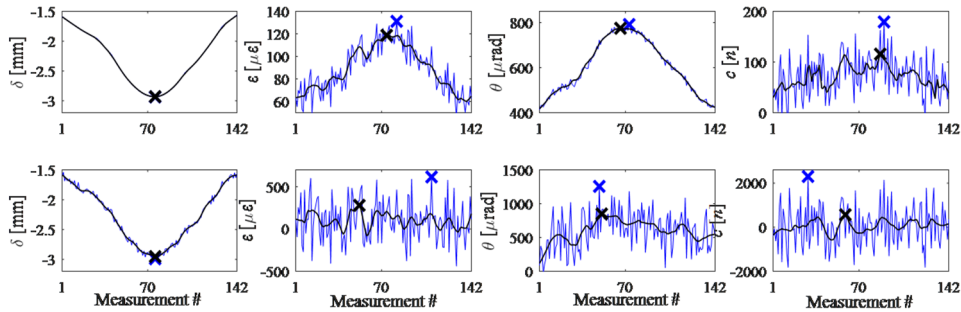


Fig. 8 From left to right: Measurement histories of raw (blue line) and pre-processed (black line) deflections, strains and curvatures at the mid-span of the girder, and inclination angles next to the left support derived from pre-processed target displacements at  $N_1F_1$  (top) and  $N_3F_1$  (bottom) combinations. ‘x’ indicates the absolute maximum response value

of noise and field of view discussed above.

### 3.5 Structural response

Maximum response values ( $r_{max}$ ) for each target location (or a set of targets) are extracted from raw and pre-processed measurements. The girder response ( $r$ ) is formed along its length. Fig. 9 shows girder response generated from both raw and pre-processed target movements at  $N_1F_1$  and  $N_3F_1$  combinations.  $r_\delta$ , at the selected scenarios, is smooth with no visible measurement error. Raw and pre-processed  $r_\epsilon$  at  $N_3F_1$  are noisy and, in contrast to  $N_1F_1$ , do not resemble the expected strain distribution at the bottom side of the girder (see Fig. 6 (top)).  $r_\theta$  at  $N_1F_1$  is similar to that of  $r_\delta$  (i.e., very smooth with no visible measurement noise), but at  $N_3F_1$  it is noisy. A drop (or measurement shift), which may result in a false damage detection, at pre-processed  $r_\theta$  is observed at the mid-span of the girder for the both combinations of measurement noise and field of view. Such trend can be related to the computation of the response, in which the maximum absolute response value at each measurement node (i.e., target) are selected, therefore resulting in a relatively large difference for the two targets at the mid-span of the girder. Both raw and pre-processed  $r_c$  at  $N_1F_1$  and  $N_3F_1$  are noisy. Only  $r_c$  at  $N_1F_1$  vaguely resembles the

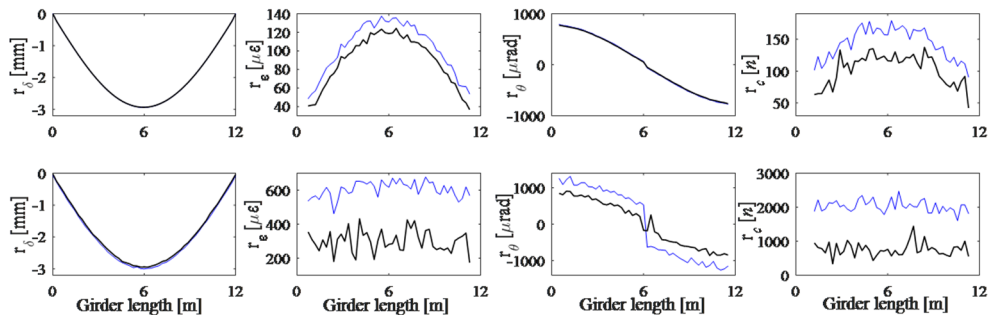


Fig. 9 Girder response ( $r$ ) from raw (blue line) and pre-processed (black line)  $r_{max}$  values at  $N_1F_1$  (top) and  $N_3F_1$  (bottom) combinations. From left to right: deflection ( $r_\delta$ ), strain ( $r_\epsilon$ ), inclination angle ( $r_\theta$ ) and curvature ( $r_c$ )

expected girder curvature (see Fig. 6 (top)). The same approach is employed to compute girder response for all other damage scenarios at all combinations of measurement noise and camera field of view.

### 3.6 Damage detection from noisy measurements

Damage detection is performed on the pre-processed girder response ( $r$ ). Damage scenario  $S_3D_5$  at  $N_1F_1$  and  $N_3F_1$  combinations is selected as the demonstrator. Fig. 10 shows plots of the change in girder response ( $\Delta r$ ) and damage feature ( $e$ ). Fig. 9 suggests that only  $r_\delta$  is marginally affected at  $N_3F_1$ . The measurement noise for the other types of response is significant enough to hide damage. This is also discernible in  $\Delta r$  plots (in Fig. 10 (top)), although  $\Delta r_\varepsilon$  has identifiable peaks at damage locations.  $\Delta r$  plots at  $N_1F_1$  are much clearer than at  $N_3F_1$  and resemble  $\Delta r$  plots in Fig. 6 (middle). Damage locations are marked either by spikes ( $\Delta r_\varepsilon$ ,  $\Delta r_c$ ,  $\Delta r_\delta$ ) or shifts ( $\Delta r_\theta$ ) in  $\Delta r$  plots.

$e_\delta$  values for the selected scenario exceed damage threshold and spike at damage locations.  $e_\varepsilon$  spikes at damage locations, however measurement noise affects the reliability of damage detection. The damage threshold is surpassed at undamaged locations, especially at  $N_3F_1$ .  $e_\theta$  at  $N_3F_1$  is very strongly affected by measurement noise. The values exceed damage threshold across the entire length of the girder. However,  $e_\theta$  at  $N_1F_1$  has very little noise, which make damage

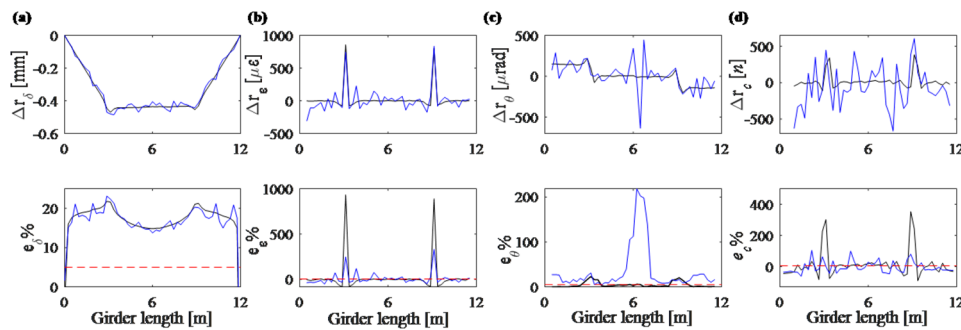


Fig. 10  $\Delta r$  and  $e$  for deflection, inclination, strain and curvature (from left to right) at damage scenarios  $S_3D_5$  at  $N_1F_1$  (black lines) and  $N_3F_1$  (blue lines) combinations. Red dashed line is the damage threshold

Table 4 Damage detection performance at added measurement noise

Damage severity	$e$	Noise and field of view combinations	$D_1$	$D_2$	$D_3$	$D_4$	$D_5$
$S_1$	$e_\varepsilon$	$N_1F_1/N_1F_2/N_2F_1/N_3F_1$	Y/N/N/N	Y/N/N/N	Y/N/N/N	Y/N/N/N	Y/N/N/N
$S_1, S_2$	$e_\delta, e_\theta, e_c$	All	N	N	N	N	N
$S_2$	$e_\varepsilon$	$N_1F_1/N_1F_2/N_2F_1/N_3F_1$	Y/Y/N/N	Y/Y/N/N	Y/Y/N/N	Y/Y/N/N	Y/Y/N/N
$S_3$	$e_\delta, e_\varepsilon$	All	Y	Y	Y	Y	Y
$S_3$	$e_\theta$	$N_1F_1/N_1F_2/N_2F_1/N_3F_1$	Y/Y/N/N	Y/Y/N/N	Y/Y/N/N	Y/Y/N/N	Y/Y/N/N
$S_3$	$e_c$	$N_1F_1/N_1F_2/N_2F_1/N_3F_1$	Y/N/Y/Y	Y/N/Y/Y	Y/N/Y/Y	Y/N/Y/Y	Y/N/Y/Y

N – damage not detected; Y – damage detected;

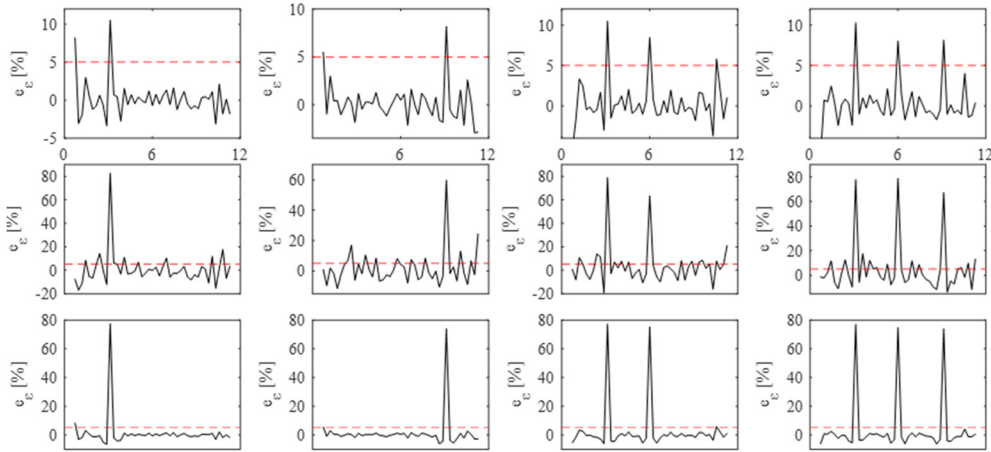


Fig. 11  $e_c$  for damage location scenarios  $D_1$ ,  $D_3$ ,  $D_4$ , and  $D_6$  (left to right) at damage severity  $S_1$  at  $N_1F_2$  (top), and  $S_2$  at  $N_1F_1$  (middle) and  $N_1F_2$  (bottom)

locations identifiable, and its values seldom exceed the damage threshold. The effect of added measurement noise is severely affecting damage detection using  $e_c$  at  $N_1F_1$  and  $N_3F_1$ .  $e_c$  values frequently exceed the damage threshold.

Damage detection performance for all damage scenarios at all combinations of added measurement noise and camera field of view are summarized in Table 4. At low damage severities (i.e.,  $S_1$  and  $S_2$ ) damages and their locations are detected only in strain measurements, when measurement noise is low ( $N_1F_1$  and  $N_1F_2$ ). Damage and its location(s) are detected from strain and displacement measurements at all combinations of measurement noise and camera field of view at damage severity  $S_3$ . Inclination angles and curvatures ( $e_\theta$  and  $e_c$ ) do not provide such good damage detection results.

Fig. 11 plots  $e_c$  values for damage scenarios, which are not presented previously, and combinations of measurement noise and field of view, at which damages and their location are detected. Even at  $N_1F_1$  damages can be detected at  $S_2$ , although, at  $S_2D_4$   $e_c$  values exceed the damage threshold slightly at no damage location.

## 4. Discussion

Findings from the numerical study and considerations for field applications of cost effective computer vision-based measurement are discussed.

### 4.1 Damage detection in numerical simulations

Target (nodal) displacements are used to compute response measurement histories from simulations of truck passages over the girder, when it is in healthy and damaged conditions. The absolute maximum response values of each target are selected to form girder response along its length. Damage sensitive features, which are derived from baseline and current girder response, are plotted along the length of the girder. In positions, where damage features exceed the damage threshold, which in this study is set at 5%, a damage is detected and located. Damage locations are

clearly discernible from damage feature plots, although they may not exceed the threshold. However, when the measurement noise is added to target displacements, damage detection is challenging, requiring pre-processing of target displacements before the derivation of response.

Damage features computed directly from target displacements (deflections) are less sensitive to low severity damages than features computed from derivatives of target displacements (inclination angles, strains and curvatures) and breach the damage threshold only when damage severity is high (see Table 2). However, damages can be clearly discernible from the plots of damage features from deflections (for example, see Fig. 6).

Damage features from strains are the most robust to noise, and small damages can be detected and accurately located (see Fig. 11). Although the girder response from inclination angles seems much smoother than that of curvatures, results in Table 4 show that damage features from curvatures detect more damage cases. This is related to the computation of damage feature from inclination angles. Damage features are computed to detect shifts rather than spikes in inclination angles. Damage features are derived from their neighbouring response (inclination angle) values (see Eqs. (9), (10), and (11)). Small values of neighbouring responses, especially when contaminated with measurement noise, result in high damage feature, leading to false damage location (see Fig. 10).

#### 4.2 Vision-based measurement challenges in field applications

The success of vision-based measurement gaining trust in the engineering community lays within its ability to offer accurate and cost effective measurement of bridge response. Affordable cameras and open source image processing tools makes vision measurement an attractive option for short term measurement collection (Feng and Feng 2016, Dong and Catbas 2020). The challenge is to accurately capture sub-pixel movements of targets, which are influenced by many factors. A few of them being (i) camera resolution, (ii) camera or ground motion, (iii) environmental conditions, and (iv) target tracking algorithm. Having a stationary reference target in the camera field of view (or background) may help removing measurement error induced by camera motion subtraction (Luo *et al.* 2018, Dong *et al.* 2020b). Capturing traffic-induced response along the entire superstructure (i.e., deck) may require multiple cameras even for a short span bridge (Dong *et al.* 2020a). When bridge dynamic response is collected, then cameras have to be time- synchronised (Lydon *et al.* 2018). The techniques proposed in this paper do not require time synchronisation of vision measurement since the absolute maximum response at a target(s) location is selected as a damage feature. Besides for accurate and repeatable measurement at each event (e.g., annual inspections) cameras do not need to be placed in the same locations to the bridge providing that pixel motions are correctly converted to engineering units (e.g., mm,  $\mu\epsilon$ ).

Even for short span bridges, desirable measurement accuracies can be achieved only when cameras are close to the target or enhanced with zoom lenses. Scaling up distributed measurement collection of long-span bridges brings additional challenges. Long-span bridges are usually very important links in the transport network. Their closures or collapses, in the worst scenario, result in significant economic losses. For example, a one-day closure of a carriageway in Scotland can cost up to £650,000 (Hannan 2015), therefore the closure of the Forth Road Bridge in Edinburgh, UK, after finding structural faults in 2015, for a duration of almost three weeks, resulted in major losses of the Scottish economy. As mentioned in Introduction, many of these important structures are equipped with a dense sensor network for timely fault/damage detection. The usual case for deflection monitoring for long-span bridges is Global Positioning System (GPS) (Brownjohn *et al.*

2015). Vision measurements were taken as benchmark when evaluating a data fusion method for accurate deflections at a mid-span of a suspension bridge using GPS and acceleration data (Xu *et al.* 2017). Increasing the number of high-end professional cameras could enable collection of distributed measurements. However, the proposed CV-SHM approach requires bridge crossings with a load truck (or a known moving load), considering the usually traffic on large bridges, this would be expensive to organize. A forward look on CV-SHM is to develop autonomous and intelligent vision-based systems composed of robotic cameras (Kromanis and Forbes 2019), which are programmed to capture desired targets on the structure at triggering events such as crossings of heavy vehicles, which, for example, can also be detected with CCTV cameras. Readers are advised to have an insight into “A forward look for CV-SHM” in a review paper by Dong and Catbas (2020).

## 5. Conclusions

A combination of cost effective cameras and available image processing algorithms for the derivation of structural response could become an affordable SHM system, which can complement regular visual inspections of small to medium span bridges. Damage detection techniques can then be applied to analyse measured response for anomalies indicating damages. This study lays the foundation for damage detection techniques for computer vision-based SHM (CV-SHM) of bridges and evaluates its feasibility on numerical simulations. A concrete girder is modelled. Crossings of a load truck are simulated for a range of damage scenarios. Nodal displacements, which are targets in vision measurement, of the girder are obtained. Measurement noise, which is a combination of the camera field of view and image processing algorithms, is added to target displacements before the computation of structure’s response (deflection, strain, inclination angle and curvature) and damage sensitive features. In addition to already known factors that influence damage detection such as (i) type of response, (ii) damage intensity, (iii) measurement noise, and (iv) damage location, the following conclusions are drawn:

- High measurement resolution is crucial for CV-SHM of bridges. Small damages can be detected, when no measurement noise is present, which is not the case in real world applications. Either achieving 1/500<sup>th</sup> pixel resolution (PR) with a fewer cameras or 1/100<sup>th</sup> PR with many more cameras is desirable for accurate response measurement.
- The proposed damage detection techniques do not require a synchronized measurement collection, when multiple cameras are employed. Only the absolute maximum response values, which are extracted from influence lines, are need to derive bridge response.
- Pre-processing target displacement histories is required to derive accurate structural response, from which bridge response and damage sensitive features are calculated.
- Damage sensitive features derived from strains are found to outperform other types of structural response. At high PRs small damages (i.e., 2.5% stiffness reduction) can be detected. Strains are unitless and calculated from movements of two targets, therefore requiring no scaling, and thus making them a good option for field applications, providing that high PR is achieved.

Future research will evaluate the proposed damage detection techniques on measurements from a laboratory setup. The setup will include a beam (undamaged and damaged), moving load and camera system. Work is also underway to elaborate damage detection and localisation for strain

measurements, which outperform other types of structural response.

### Author Contributions

CBO generated the numerical model and analysed the data. RK validated the accuracy of the numerical model. Both authors contributed to the writing.

### Conflicts of Interest

The authors declare no conflict of interest.

### References

- Abdo, M. A.-B. (2011), "Parametric study of using only static response in structural damage detection", *Eng. Struct.*, **34**, 124-131. <https://doi.org/10.1016/j.engstruct.2011.09.027>
- ANSYS (2018), ANSYS Mechanical APDL Element Reference, in Help System, 1377-1390. [www.ansys.com](http://www.ansys.com)
- Bakhtiari-Nejad, F., Rahai, A. and Esfandiari, A. (2005), "A structural damage detection method using static noisy data", *Eng. Struct.*, **27**, 1784-1793. <https://doi.org/10.1016/J.ENGSTRUCT.2005.04.019>
- Brownjohn, J.M.W. (2007), "Structural health monitoring of civil infrastructure", *Philos. Trans. R. Soc. a-Mathe. Phys. Eng. Sci.*, **365**(1851), 589-622. <https://doi.org/10.1098/rsta.2006.1925>
- Brownjohn, J.M.W., Koo, K.Y., Scullion, A. and List, D. (2015), "Operational deformations in long-span bridges", *Struct. Infrastruct. Eng.*, **11**, 556-574. <https://doi.org/10.1080/15732479.2014.951857>
- Brownjohn, J.M.W., Kripakaran, P., Harvey, B., Kromanis, R., Jones, P. and Huseynov, F. (2016), "Structural Health Monitoring of short to medium span bridges in the United Kingdom", *Struct. Monit. Maint., Int. J.*, **3**(3), 259-276. <https://doi.org/10.12989/smm.2016.3.3.259>
- Brownjohn, J.M.W., Xu, Y. and Hester, D. (2017), "Vision-Based Bridge Deformation Monitoring", *Front. Built Environ.*, **3**, 1-16. <https://doi.org/10.3389/fbuil.2017.00023>
- Chen, X., Hong-ping, Z. and Chuan-yao, C. (2005), "Structural damage identification using test static data based on grey system theory", *J. Zhejiang Univ. A*, **6**, 790-796. <https://doi.org/10.1631/jzus.2005.A0790>
- Chu, X., Zhou, Z., Deng, G., Duan, X. and Jiang, X. (2019), "An overall deformation monitoring method of structure based on tracking deformation contour", *Appl. Sci.*, **9**(21), 4532. <https://doi.org/10.3390/app9214532>
- Dalia, Z.M., Bagchi, S., Sabamehr, A., Bagchi, A. and Bhowmick, A. (2018), "Life cycle cost-benefit analysis of SHM of I-35 W St. Anthony Falls bridge", In: *International Symposium on Structural Health Monitoring and Nondestructive Testing*, Saarbruecken, Germany, October.
- Doebling, S.W., Farrar, C.R. and Prime, M.B. (1998), "A summary review of vibration-based damage identification methods", *Shock Vib. Dig.*, **30**, 91-105.
- Dong, C.-Z. and Catbas, F.N. (2020), "A review of computer vision-based structural health monitoring at local and global levels", *Struct. Heal. Monit.*, **1**. <https://doi.org/10.1177/1475921720935585>
- Dong, C.Z., Bas, S. and Catbas, F.N. (2020a), "A portable monitoring approach using cameras and computer vision for bridge load rating in smart cities", *J. Civil Struct. Heal. Monit.*, **10**, 1001-1021. <https://doi.org/10.1007/s13349-020-00431-2>
- Dong, C.Z., Celik, O., Catbas, F.N., O'Brien, E.J. and Taylor, S. (2020b), "Structural displacement monitoring using deep learning-based full field optical flow methods", *Struct. Infrastruct. Eng.*, **16**, 51-71. <https://doi.org/10.1080/15732479.2019.1650078>
- Erdenebat, D. and Waldmann, D. (2020), "Application of the DAD method for damage localisation on an

- existing bridge structure using close-range UAV photogrammetry”, *Eng. Struct.*, **218**, 110727.  
<https://doi.org/10.1016/j.engstruct.2020.110727>
- Erdenebat, D., Waldmann, D., Scherbaum, F. and Teferle, N. (2018), “The Deformation Area Difference (DAD) method for condition assessment of reinforced structures”, *Eng. Struct.*, **155**, 315-329.  
<https://doi.org/10.1016/j.engstruct.2017.11.034>
- Erdenebat, D., Waldmann, D. and Teferle, N. (2019), “Curvature based DAD-method for damage localisation under consideration of measurement noise minimisation”, *Eng. Struct.*, **181**, 293-309.  
<https://doi.org/10.1016/j.engstruct.2018.12.017>
- Feng, D. and Feng, M.Q. (2016), “Output-only damage detection using vehicle-induced displacement response and mode shape curvature index”, *Struct. Control Health Monitor.*, **23**, 1088-1107.  
<https://doi.org/10.1002/stc>
- Feng, D. and Feng, M.Q. (2018), “Computer vision for SHM of civil infrastructure: From dynamic response measurement to damage detection – A review”, *Eng. Struct.*, **156**, 105-117.  
<https://doi.org/10.1016/j.engstruct.2017.11.018>
- Feng, D., Feng, M.Q., Ozer, E. and Fukuda, Y. (2015), “A vision-based sensor for noncontact structural displacement measurement”, *Sensors*, **15**, 16557-16575. <https://doi.org/10.3390/s150716557>
- Fukuda, Y., Feng, M.Q., Narita, Y. and Tanaka, T. (2013), “Vision-based displacement sensor for monitoring dynamic response using robust object search algorithm”, *IEEE Sens. J.*, **13**, 4725-4732.  
<https://doi.org/10.1109/JSEN.2013.2273309>
- Gauthier, J.F., Whalen, T.M. and Liu, J. (2008), “Experimental validation of the higher-order derivative discontinuity method for damage identification”, *Struct. Control Health Monitor.*, **15**, 143-161.  
<https://doi.org/10.1002/stc.210>
- Hannan, M. (2015), “Forth Road Bridge closure will have huge impact on Scottish economy”.  
 Available at: <http://www.thenational.scot/news/forth-road-bridge-closure-will-have-huge-impact-on-scottish-economy.10831> [Accessed January 26, 2016]
- Highways Agency, Scottish Executive Development Department, The National Assembly for Wales, and Department for Regional Development (2018), Design Manual for Roads and Bridges, 3.
- Imetrum (2020), Digital Image Correlation.  
 Available at: <https://www.imetrum.com/products/digital-image-correlation/> [Accessed February 2, 2020]
- Ji, X., Miao, Z. and Kromanis, R. (2020), “Vision-based measurements of deformations and cracks for RC structure tests”, *Eng. Struct.*, **212**, 110508. <https://doi.org/10.1016/j.engstruct.2020.110508>
- Khuc, T. and Catbas, F.N. (2017), “Computer vision-based displacement and vibration monitoring without using physical target on structures”, *Struct. Infrastruct. Eng.*, **13**, 505-516.  
<https://doi.org/10.1080/15732479.2016.1164729>
- Kromanis, R. (2020), “Health monitoring of bridges”, In: *Start-Up Creation*, eds. F. Pacheco-Torgal, E. Rasmussen, C.-G. Granqvist, V. Ivanov, A. Kaklauskas, and S. Makonin (Elsevier Ltd.), pp. 369-389.  
<https://doi.org/10.1016/b978-0-12-819946-6.00014-x>
- Kromanis, R. and Al-Habaibeh, A. (2017), “Low cost vision-based systems using smartphones for measuring deformation in structures for condition monitoring and asset management”, *Proceedings of SHMII 2017 - 8th International Conference on Structural Health Monitoring of Intelligent Infrastructure*, (International Society for Structural Health Monitoring of Intelligent Infrastructure, ISHMII), pp. 430-440.
- Kromanis, R. and Forbes, C. (2019), “A Low-Cost Robotic Camera System for Accurate Collection of Structural Response”, *Inventions*, **4**, 47. <https://doi.org/10.3390/inventions4030047>
- Kromanis, R. and Liang, H. (2018), “Condition assessment of structures using smartphones: a position independent multi-epoch imaging approach”, *Proceedings of the 9th European Workshop on Structural Health Monitoring Series (EWSHM)*, Manchester, UK.  
<http://www.ultrasonic.de/article/ewshm2018/papers/0082-Kromanis.pdf>
- Kromanis, R., Xu, Y., Lydon, D., Martinez del Rincon, J. and Al-Habaibeh, A. (2019), “Measuring structural deformations in the laboratory environment using smartphones”, *Front. Built Environ.*, **5**, p. 44.  
<https://doi.org/10.3389/fbuil.2019.00044>
- Lee, E.T. and Eun, H.C. (2008), “Damage detection of damaged beam by constrained displacement

- curvature”, *J. Mech. Sci. Technol.*, **22**, 1111-1120. <https://doi.org/10.1007/s12206-008-0310-3>
- Luo, L., Feng, M.Q. and Wu, Z.Y. (2018), “Robust vision sensor for multi-point displacement monitoring of bridges in the field”, *Eng. Struct.*, **163**, 255-266. <https://doi.org/10.1016/j.engstruct.2018.02.014>
- Lydon, D., Lydon, M., del Rincón, J.M., Taylor, S.E., Robinson, D., O’Brien, E. and Catbas, F.N. (2018), “Development and field testing of a time-synchronized system for multi-point displacement calculation using low-cost wireless vision-based sensors”, *IEEE Sens. J.*, **18**, 9744-9754. <https://doi.org/10.1109/JSEN.2018.2853646>
- Lydon, D., Lydon, M., Taylor, S., Del Rincon, J.M., Hester, D. and Brownjohn, J. (2019), “Development and field testing of a vision-based displacement system using a low cost wireless action camera”, *Mech. Syst. Signal Process.*, **121**, 343-358. <https://doi.org/10.1016/j.ymsp.2018.11.015>
- Park, J.C., Cho, J.S., Gil, H.B. and Shin, J.I. (2015), “Measurement and evaluation of thermal movements of existing bridges using a series of two-dimensional images”, *Proceedings of the 7th International Conference on Structural Health Monitoring of Intelligent Infrastructure*, Torino, Italy, pp. 1378-1385.
- Potter, K.D. and Setchell, C. (2014), “Positional measurement of a feature within an image”, U.S. Patent 8,718,403.
- Reagan, D., Sabato, A. and Niezrecki, C. (2018), “Feasibility of using digital image correlation for unmanned aerial vehicle structural health monitoring of bridges”, *Struct. Health Monitor.*, **17**, 1056-1072. <https://doi.org/10.1177/1475921717735326>
- Ri, S., Tsuda, H., Chang, K., Hsu, S., Lo, F. and Lee, T. (2020), “Dynamic deformation measurement by the sampling Moiré method from video recording and its application to bridge engineering”, *Exp. Tech.*, 1-15. <https://doi.org/10.1007/s40799-019-00358-4>
- Ribeiro, D., Calçada, R., Ferreira, J. and Martins, T. (2014), “Non-contact measurement of the dynamic displacement of railway bridges using an advanced video-based system”, *Eng. Struct.*, **75**, 164-180. <https://doi.org/10.1016/j.engstruct.2014.04.051>
- Shao, S., Zhou, Z., Deng, G., Du, P., Jian, C. and Yu, Z. (2020), “Experiment of Structural Geometric Morphology Monitoring for Bridges Using Holographic Visual Sensor”, *Sensors*, **20**, 1-25. <https://doi.org/10.3390/s20041187>
- Transport for London (2011), Hammersmith flyover to remain closed next week - Transport for London.
- Xu, Y. and Brownjohn, J.M.W. (2017), “Review of machine-vision based methodologies for displacement measurement in civil structures”, *J. Civil Struct. Health. Monitor.*, **8**, 91-110. <https://doi.org/10.1007/s13349-017-0261-4>
- Xu, Y., Brownjohn, J.M.W., Hester, D. and Koo, K.Y. (2017), “Long-span bridges: Enhanced data fusion of GPS displacement and deck accelerations”, *Eng. Struct.*, **147**, 639-651. <https://doi.org/10.1016/j.engstruct.2017.06.018>
- Xu, Y., Brownjohn, J. and Kong, D. (2018), “A non-contact vision-based system for multipoint displacement monitoring in a cable-stayed footbridge”, *Struct. Control Health Monitor.*, **25**, 1-23. <https://doi.org/10.1002/stc.2155>
- Zaurin, R. and Catbas, F.N. (2010), “Integration of computer imaging and sensor data for structural health monitoring of bridges”, *Smart Mater. Struct.*, **19**, 015019. <https://doi.org/10.1088/0964-1726/19/1/015019>
- Zhou, H., Dai, F. and Lu, L. (2019), “Temperature-induced error in long-term continuous monitoring of displacement with videogrammetry”, In: *Winter Simulation Conference (WSC) (IEEE)*, National Harbor, MD, USA, December, pp. 2986-2991.